The Journal of Physiology

Morphology, physiology and synaptic connectivity of local interneurons in the mouse somatosensory thalamus

Jane Simko[1] and Henry Markram[1,2]

[1]*Laboratory of Neural Microcircuitry, Brain Mind Institute, School of Life Sciences, École Polytechnique Fédérale de Lausanne (EPFL), Lausanne, Switzerland*
[2]*Blue Brain Project, École Polytechnique Fédérale de Lausanne (EPFL), Campus Biotech, Geneva, Switzerland*

Edited by: Katalin Toth & Jean-Claude Béïque

The peer review history is available in the Supporting Information section of this article (https://doi.org/10.1113/JP281711#support-information-section).

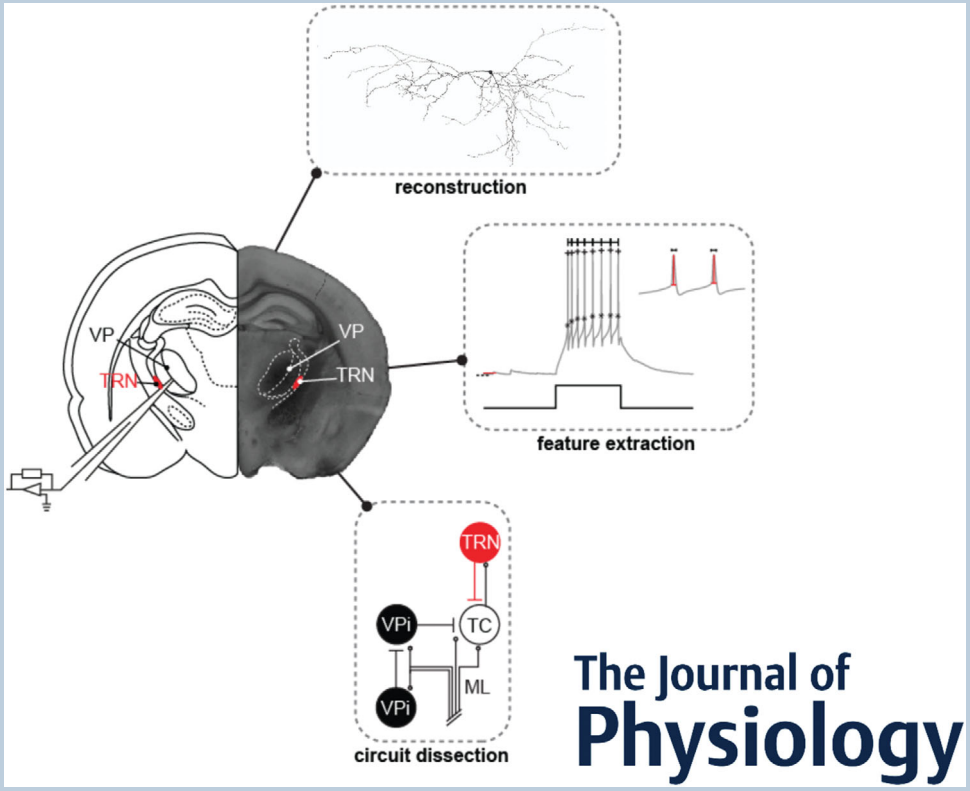

Abstract The thalamic reticular nucleus (TRN) neurons, projecting across the external medullary lamina, have long been considered to be the only significant source of inhibition of the somatosensory ventral posterior (VP) nuclei of the thalamus. Here we report for the first time effective local inhibition and disinhibition in the VP. Inhibitory interneurons were found in

Jane Simko completed her doctorate in 2021 at the École Polytechnique Fédérale de Lausanne with Professor Henry Markram studying thalamic circuitry and the physiology of somatosensory thalamic interneurons using multiple patch clamp strategies. She is now a postdoctoral research fellow at Columbia University with Professor Christopher Makinson. Her research interests involve using interdisciplinary approaches to investigate biophysical mechanisms of neuronal coding and computation in sensory systems.

DOI: 10.1113/JP281711

GAD67–GFP-expressing mice and studied using *in vitro* multiple patch clamp. Inhibitory interneurons have expansive bipolar or tripolar morphologies, reach across most of the VP nucleus and display low threshold bursting behaviour. They form triadic and non-triadic synaptic connections onto thalamocortical relay neurons and other interneurons, mediating feedforward inhibition and disinhibition. Synaptic inputs arrive before those expected from the TRN neurons, suggesting that local inhibition plays an early and significant role in the functioning of the somatosensory thalamus.

(Received 27 April 2021; accepted after revision 28 September 2021; first published online 30 September 2021)
Corresponding author H. Markram: Brain Mind Institute, École Polytechnique Fédérale de Lausanne (EPFL), Lausanne, Vaud 1015, Switzerland. Email: henry.markram@epfl.ch

Abstract figure legend The physiology and morphology of local thalamic interneurons of the mouse somatosensory thalamus have not previously been studied. Using *in vitro* multiple patch clamp electrophysiology strategies, we have reconstructed 3D morphologies, extracted active and passive electrophysiological features, and dissected their sophisticated microcircuitry. Our findings suggest a significant role for local interneurons in canonical thalamic functions including sensory perception and sleep.

Key points

- The physiology and structure of local interneurons in the mouse somatosensory thalamus is described for the first time.
- Inhibitory interneurons have extensive dendritic arborization providing significant local dendro-dendritic inhibition in the somatosensory thalamus.
- Triadic and non-triadic synaptic connectivity onto thalamic relay neurons and other interneurons provides both local feedforward inhibition and disinhibition.
- Interneurons of the somatosensory thalamus provide inhibition before the thalamic reticular nucleus, suggesting they play an important role in sensory perception.

Introduction

The excitatory thalamocortical neurons of the rodent sensory thalamus rarely form intranuclear recurrent connections (Lee *et al.* 2010), leaving thalamic local interneurons to play the primary role in shaping the spatial and temporal features of incoming information (Sherman, 2004; Wang *et al.* 2011; Martinez *et al.* 2014; Hirsch *et al.* 2015). Thalamic interneurons contain synaptic vesicles in their dendrites (Hamos *et al.* 1985; Morgan & Lichtman, 2020) that support dendro-dendritic synapses (Hamos *et al.* 1985). Further, electron microscopy studies have shown that interneuron dendrites together with thalamocortical neuron dendrites and retinal ganglion cell afferents form triadic synapses (Hamos *et al.* 1985; Morgan & Lichtman, 2020). This triadic arrangement allows for fast feedforward inhibition with a reliable delay of approximately 1 ms (Blitz & Regehr, 2005), sharpening the temporal precision of incoming sensory input (Casti *et al.* 2008; Babadi *et al.* 2010; Butts *et al.* 2011) and controlling the gain of sensory information (Sherman, 2004; Heiberg *et al.* 2016). A diversity of other synaptic motifs has also been reported including autaptic synapses, interneuron–interneuron–thalamocortical triadic synapses, interneuron–interneuron reciprocal synapses, and interneuron–thalamocortical connections with no other input nearby (non-triadic; Morgan & Lichtman, 2020).

Thalamic interneurons have been almost exclusively studied in the rodent visual thalamic nucleus, the dorsal lateral geniculate nucleus (dLGN), where they are found in sufficiently large numbers (5.6–20% of dLGN neurons) to play a major role in LGN processing (Arcelli *et al.* 1997; Cavdar *et al.* 2014; Evangelio *et al.* 2018). Thalamic interneurons are known to be present in the rodent somatosensory ventral posterior nucleus (VP), comprising the ventral posteromedial (VPM) and ventral posterolateral (VPL) thalamic nuclei receiving inputs from the face and body, respectively (Lund & Webster, 1967; Dörfl, 1985; Arcelli *et al.* 1997; Pierret *et al.* 2000; Veinante *et al.* 2000; Cavdar *et al.* 2014; Jager *et al.* 2016; Evangelio *et al.* 2018), but since they only constitute 1–4.2% of VP neurons, their role has been overlooked. Furthermore, the lower percentage of thalamic interneurons in the VP is a trait unique to rodents as other mammalian species tend to have much higher proportions (Arcelli *et al.* 1997). Instead, the

reticular nucleus in rodents has been considered as the primary source of inhibition in the VP (Pinault, 2004). The interneurons of the VP (VPi) have therefore not yet been morphologically and electrically characterized, their synaptic connectivity has remained unknown and their role in sensory processing has not been appreciated. Here we provide the first detailed characterization of the mouse VP interneurons, the synaptic connections they form and their impact on the thalamocortical (TC) neurons during external input.

VP interneurons have expansive bipolar or tripolar morphologies and display low threshold bursting firing behaviour. They form triadic and non-triadic circuit motifs that provide significant feedforward inhibition and disinhibition with short delays, suggesting that VP interneurons could enrich the somatosensory thalamus with a higher level of processing than previously considered.

Methods

Ethical approval

All experiments and procedures were in strict adherence to the Swiss national and institutional guidelines and were performed under a license granted by local canton Veterinary Authorities (License number: VD3458).

Animals

Animals were bred at the École Polytechnique Fédérale de Lausanne, group-housed (max 5 per cage), on a 12 h light–dark cycle. Food and water were provided *ad libitum*. Initial GAD67-GFP breeders were obtained from the lab of Takeshi Kaneko (Tamamaki *et al.* 2003). Mice were fully backcrossed with C57BL/6 mice. A total number of 103 cells from 52 11- to 33-day-old GAD67-GFP mice, both male (27 mice) and female (25 mice), were included in this study.

Slice preparation and solutions

GAD67-GFP mice were quickly decapitated without sedation to prevent any effects of anaesthetic agents on electrophysiological recordings. Brains were placed in artificial cerebral spinal fluid (aCSF). Coronal and horizontal slices (300 μm) containing the VP were cut on a vibratome (Leica VT1200 S, Leica Microsystems, Wetzlar, Germany) in sucrose cutting solution containing (mM): 2.6 KCl, 10 $MgCl_2$, 0.5 $CaCl_2$, 1.27 NaH_2PO_4, 26 $NaHCO_3$, 200 sucrose and 10 glucose. Slices were then transferred to aCSF containing (mM): 125 NaCl, 25 $NaHCO_3$, 2.5 KCl, 1.25 NaH_2PO_4, 2 $CaCl_2$, 1 $MgCl_2$ and 25 D-glucose bubbled with 95% O_2–5% CO_2. Slices were incubated in 34 $\pm$ 1°C for 30 min before resting at room temperature prior to the experiment. Regular pipette intracellular solution contained (mM): 110 potassium gluconate, 10 KCl, 4 ATP-Mg, 10 phosphocreatine, 0.3 GTP, 10 HEPES and 8.1 biocytin adjusted to pH 7.3–7.4 with KOH. Voltage clamp recordings were performed with (mM): 135 caesium gluconate, 5 NaCl, 0.5 EGTA, 10 HEPES, 2 $MgSO_4$, 0.16 $CaCl_2$, 4 Na_2ATP, 0.4 NaGTP, 14 phosphocreatine and 8.1 biocytin adjusted to pH 7.3–7.4 with CsOH. Osmolarity was adjusted to 290–300 mOsm.

Electrophysiology

VPis were located using the presence of green fluorescent protein (GFP) fluorescence under the endogenous GAD67 gene promoter. Cells were targeted approximately ~20–100 μm from the slice surface. Up to four simultaneous patch-clamp micromanipulators were controlled using a computer-assisted multi-electrode patch-clamp system written in custom C++ code (Perin & Markram, 2013). Recordings were performed in whole-cell mode with Multineuron patch-clamp 200 B amplifiers (Molecular Devices, San Jose, CA, USA) in the current clamp or voltage clamp mode at 34 $\pm$ 1°C bath temperature. Data acquisition was performed through an ITC-1600 board (HEKA Elektronik, Lambrecht (Pfalz), Germany) connected to a PC running a custom-written routine (PulseQ) under IGOR Pro (WaveMetrics, Lake Oswego, OR, USA). Recordings were sampled at 5 kHz, and the voltage signal was filtered with a 2-kHz Bessel filter. Patch pipettes were pulled with a Flaming/Brown micropipette puller, P-97 (Sutter Instrument Co., Novato, CA, USA) and had an initial resistance of 3–8 MΩ. In voltage clamp experiments, slow and fast capacitive components were compensated. Series resistance was monitored throughout the experiments. Series resistance exceeding 25 MΩ were not used for analysis. The membrane potential values given were not corrected for the liquid junction potential, which is approximately −14 mV. Various experiments involving extracellular stimulation were performed using tungsten bipolar electrodes (World Precision Instruments, Sarasota, FL, USA) placed onto visible landmarks on the slice. Initial experiments used 3 ms bipolar stimulations with the majority of experiments using 200 μs stimulations. The medial lemniscus (ML), reticular nucleus (TRN) and internal capsule (IC) were clearly visible without the use of a microscope in horizontal slice orientations.

Histological procedures and morphological reconstruction

Slices were incubated in 2% paraformaldehyde, 0.3% picric acid and 1% glutaraldehyde solution overnight. Slice solution was then changed to phosphate-buffered saline. Slices were immersed in 3% H_2O_2 for 45 min, then 0.1%

Triton X-100 for 26 min. Slices were then incubated in 4% ABC reagent (Vector Laboratories, Burlingame, CA, USA) and 0.5% Triton X-100 for 30 min at room temperature and reacted with 3,3′-diaminobenzidine as a chromagen without nickel intensification. Neurons were examined using an Olympus (Tokyo, Japan) BX61 microscope with UPLFLN ×100 oil immersion lens and reconstructed using the Neurolucida system (MBF Bioscience, Williston, VT, USA). Putative synaptic contacts were identified with a light microscope as the crossing of two projections in the same focal plane. The location of the cells in slice were obtained by applying an affine transformation of the slice to an overlay of the Allen Mouse Brain Atlas (Allen Institute for Brain Science, 2004).

Determination of active and passive electrical properties of VPi

VPis were held at −70 mV unless otherwise noted. Current stimulation delivered to patched VPis was normalized to the rheobase current, calculated in-experiment as the current required to elicit an action potential. The following stimuli were used for analysis:

APWaveform: six depolarizing current steps from 60 to 260% at 40% increments, with a duration of 225 ms.
FirePattern: two depolarizing current steps from 120 to 200%, with a duration of 3600 ms.
IDThresh: multiple depolarizing current steps from 50 to 130% at 4% increments, with a duration of 270 ms.
IV:depolarizing and hyperpolarizing steps from 60 to 140% at 20% decrements, with a duration of 3000 ms.
IV long: hyperpolarizing and depolarizing steps of 3000 ms from 20 to 140% at 20% increments, with a longer total recording time than IV to capture rebound bursting.
SponNoHold30: no holding or stimulation currents were applied for 30 s.

Active and passive electrical properties were analysed using custom MATLAB (The MathWorks Inc., Natick, MA, USA) scripts or MATLAB functions calling a feature extraction library written in C/C++. Resting membrane potential was calculated as the mean voltage of SponNoHold30. Input resistance (R_{in}) was calculated as the slope of a current–voltage function created from using the IV stimulus by determining the steady state voltage response to each current step. The membrane time constant (tau) was calculated from a single or double exponential function fit to the decay phase of the response to the IV stimulus. Membrane capacitance (C_m) was determined from the equation $C_m = \text{tau}/R_{in}$. Voltage sag (V_{sag}) was measured from the IV stimulus only from cells that reached negative potentials of at least −95 mV in response to hyperpolarizing current steps. This value was taken manually as the approximate minimum voltage amplitude, typically reached within 200 ms, subtracted by the steady state voltage value. Action potential (AP) threshold was calculated using the voltage response corresponding to IDThresh stimulus with the criteria in which dV/dt on the AP voltage trace was greater than 12 mV/ms. The width of AP at AP-threshold was considered as AP-width using the APWaveform stimulus. AP half-width was determined by the width of the action potential at half the maximal action potential response (peak voltage). Interspike intervals with the FirePattern stimulus were calculated as the time difference between consecutive times at peak voltage.

Analysis of unitary postsynaptic potentials and postsynaptic currents

Unitary postsynaptic potentials (PSPs) and postsynaptic currents (PSCs) were analysed using MATLAB scripts. PSPs or PSCs were considered if the absolute value is >2 times the standard deviation of the baseline. Baseline was calculated as the mean of 10 ms prior to the stimulation or presynaptic action potential. Amplitudes were found at the maximum or minimum point within a 1.5–18 ms time window after the stimulation onset or time in which the presynaptic action potential passes −15 mV. Lower or upper bounds of detection windows were adjusted when necessary. The rise time was determined as the time interval encompassing 20–80% of the amplitude. Latencies were determined by calculating the onset time of the PSP or PSC and subtracting the stimulation onset or the time in which the presynaptic action potential passes −15 mV. This onset time represented the intersection of the line at baseline and the line through the 20% and 80% amplitude points. The decay time constant of the PSP or PSC was calculating by fitting a monoexponential function using a non-linear least-squares fit algorithm.

Statistics

Box plots were used consisting of the lower quartile, median and upper quartile with whiskers at the greatest data point within 1.5 times the interquartile range. All boxplots in this study had the possibility of displaying outliers set at values more than 1.5 times the interquartile range past the upper or lower quartile. Significance of difference was assessed statistically using a two-tailed Mann-Whitney test with statistical significance set at $P < 0.05$. Data are expressed as means (SD). Values were tested against a normal distribution using the Kolmogorov–Smirnov test with statistical significance set at $P < 0.05$.

Results

Morphology of VP interneurons

Mice (postnatal day 11–33) expressing GAD67–GFP were used to reveal inhibitory interneurons in the VP. We found between 5 and 20 clearly visible fluorescent interneurons in a single 300 μm-thick slice of the VP (Fig. 1*A*). Patch-clamp recordings were obtained from fluorescent neurons using biocytin-filled pipettes for subsequent histochemical staining. Computer-aided 3D reconstruction was performed on neurons that were completely ($n = 8$ cells) or partially stained ($n = 10$ cells). Their dendritic arborizations were bipolar (Fig. 1*B*) and tripolar (Fig. 1*C*). Somata that were sufficiently stained were measured ($n = 39$ cells). Somata were elongated, ranging in size from 10.2 to 21.5 μm along their polar axes (Fig. 1*B*–*D*). A test of unimodality suggests that the distribution of soma sizes does not come from a bimodal distribution (*P*-value: 0.4006; Hartigan's dip test of unimodality). However, to analyse any further significant differences due to soma size, a finite mixture model was used (Trang *et al.* 2015) to calculate the cut-off soma size to discriminate two modes of the distribution (μ_1: 12.56, σ_1: 1.28, μ_2: 17.37, σ_2: 1.96 in μm; cut-off value: 16.29 μm; Fig. 1*D*). The existence of two populations based on soma size is unclear, though this is an observation reported on interneuron sizes in the dLGN (Fig. 1*D*) (Leist *et al.* 2016).

Morphological reconstruction of the interneurons revealed extensive local dendritic arborization with comparatively smaller axon trees (Fig. 1*E* and Fig. 2). The dendritic arbours reached as much as 843 μm, extending across most of the VP (Fig. 1*E* and *F*, and Fig. 2), with diverse orientations relative to the TRN. Dendrites did not appear to respect nuclear boundaries (Fig. 1*F*); however, nucleus borders were not always distinct in slice images. Dendrites were beaded with no spines, but often had short spine-like branches. Axons were difficult to separate from dendrites under light microscopy because they resembled thinner distal dendrites (Morgan & Lichtman, 2020) and originated either from the soma or from one of the proximal dendrites (Zhu & Lo, 1999; Morgan & Lichtman, 2020). The apparent lack of a distinct and extensive axonal arborization suggests that most of the inhibition of the VP interneurons is provided via their dendrites using dendro-dendritic synapses. Even though restricted spread of biocytin in the thin axons cannot be excluded, these morphological features are consistent with those reported for interneurons in the dLGN (Zhu & Lo, 1999; Morgan & Lichtman, 2020).

Considering the density and distribution of GAD67–GFP-expressing interneurons and the expanse of their dendritic and axonal arbours, VP interneurons are anatomically well positioned to provide inhibition to all TC neurons in the VP, despite their relatively lower densities as compared to the LGN.

Electrophysiology of VP interneurons

The active and passive electrophysiological properties of VP interneurons were studied by injecting current pulses that were normalized in their amplitudes to the rheobase current amplitude (current required to reach threshold spiking) for each patched neuron ($n = 58$; Fig. 3*A*; see Methods). VP interneurons exhibited accommodating firing behaviour, typically beginning with a burst of two to five action potentials at low holding potentials (Fig. 3*B*). Strong hyperpolarization ($\sim$−95 mV) applied to 25 interneurons revealed rebound bursts in 10 (40%) of these interneurons (Fig. 3*C*), consistent with properties of interneurons that have been observed in the dLGN (Zhu *et al.* 1999*b*; Leist *et al.* 2016). Two of the recorded interneurons exhibited spontaneous oscillatory activity (Fig. 3*D*) also as previously reported in *in vitro* (Zhu *et al.* 1999*a*) and *in vivo* preparations (Deschênes *et al.* 1984) in the dLGN and VP, respectively.

Electrophysiological features were analysed using custom software programs (see Methods; Fig. 3*E*). We report no significant difference in electrophysiological features between neurons patched in the VPM or VPL nucleus (*P*-values: resting membrane potential, 0.7330; input resistance, 0.8523; tau, 0.7418; membrane capacitance, 1.000; minimum current for AP, 0.8490; AP threshold, 0.1083; first AP half-width, 0.3024; last AP half-width, 0.1413; ln(last ISI/second ISI), 0.5309; V_{sag}, 0.7396; two-tailed Mann–Whitney test; significance set to $P < 0.05$). This may suggest similar physiological mechanisms and processing across the entire VP nucleus. Though we used mice in a broad range of developmental stages (P11–33), we observed modest statistical differences in a few passive electrical properties between pre-weaned (<P21) and weaned (≥P21) groups: Resting membrane potential ($P = 0.0493$) and V_{sag} ($P = 0.0025$). It is possible that interneurons are maturing post-natally and thus undergo physiological changes during development. Other analysed features show no significant difference (*P*-values: input resistance, 0.8453; tau, 0.5454; membrane capacitance, 0.4585; minimum current for AP, 0.7052; AP threshold, 0.8566; first AP half-width, 0.3127; last AP half-width, 0.8734; ln(last ISI/second ISI), 0.4399; two-tailed Mann–Whitney test; significance set to $P < 0.05$).

VP interneurons have high input resistances (mean: 544.64 (SD: 210.31) MΩ; Fig. 3*F* and Table 1), likely due to their electrotonically extensive dendritic structures (Sherman, 2004). These interneurons display spike train adaptation calculated as the natural logarithm of the

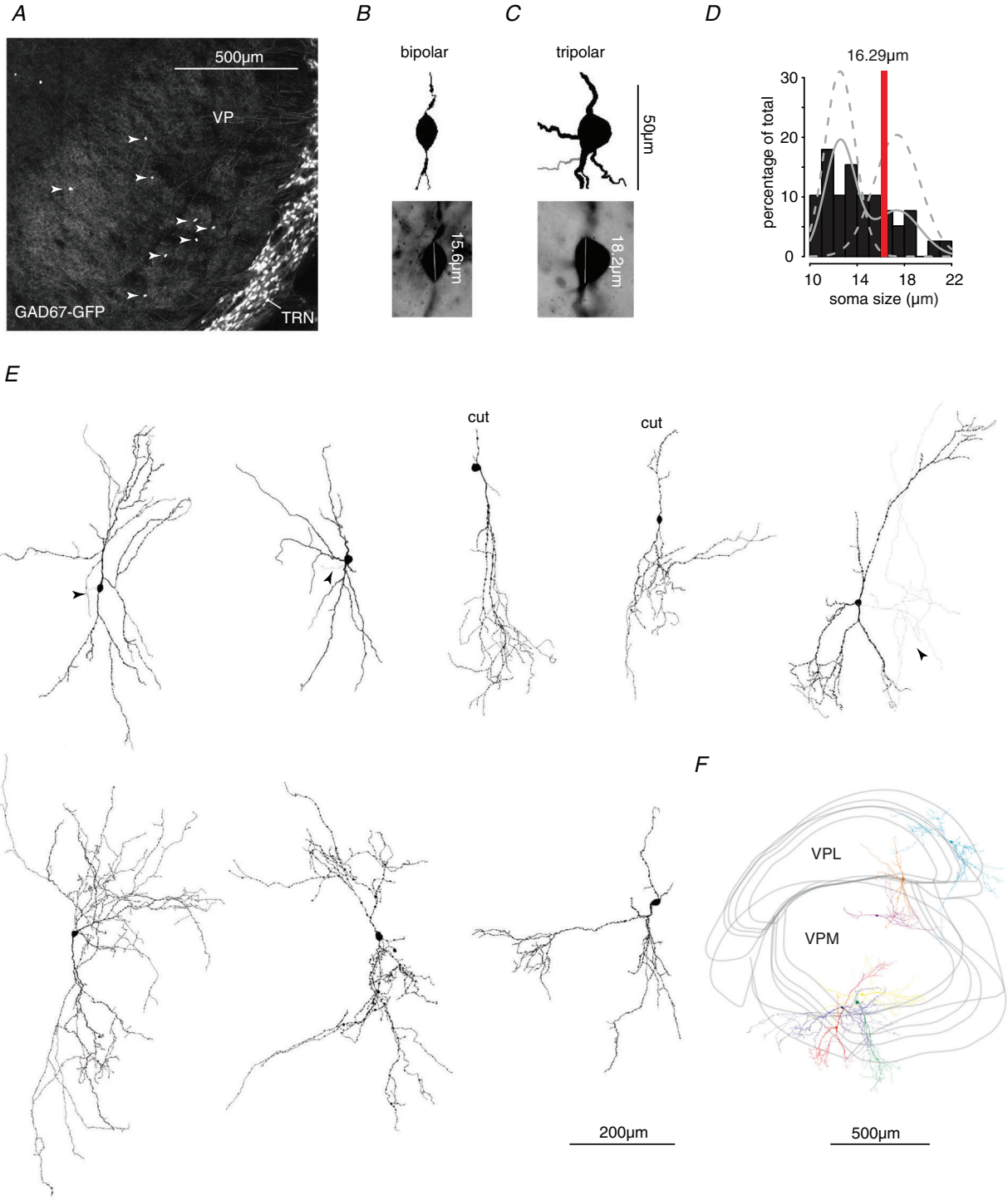

Figure 1. Morphology of VP interneurons
A, maximum projection of *z*-stack images in the VP of a GAD67-GFP mouse. Interneuron somas are marked with arrowheads. *B*, bipolar reconstructed interneuron with slice image. *C*, tripolar reconstructed interneuron with slice image. *D*, histogram of soma sizes fitted with non-parametric (continuous grey line) and finite mixture model (dashed grey line) estimations of distribution. Estimated cut-off for the bimodal distribution is in the center of the red line indicating the 97.5% confidence interval. *E*, 3D reconstructed morphologies. Likely cut major dendritic branches are noted. Putative axons are coloured in grey and also marked with arrowheads. *F*, horizontal slicing orientation outlines of the ventral posterolateral (VPL) and ventral posteromedial (VPM) nuclei overlaid with cell positions for 7 of the 8 morphologies shown. One morphology from a coronal slicing orientation was excluded in this overlay.

Table 1. Summary table of active and passive electrophysiological features

Parameter	Mean (SD)
Resting membrane potential (mV)	−60.61 (12.27)
Input resistance (MΩ)	544.64 (210.31)
Tau (ms)	34.25 (6.14)
Membrane capacitance (pF)	72.90 (28.25)
Minimum current for AP (pA)	19.80 (13.68)
AP threshold (mV)	−38.99 (5.98)
First AP half-width (ms)	1.15 (0.29)
Last AP half-width (ms)	1.27 (0.35)
ln(last ISI/second ISI)	0.97 (0.86)
V_{sag} ($V_{max} - V_{steadystate}$)	5.38 (3.37)

Summary table of 10 active and passive electrophysiological features recorded in GAD67-GFP mice. Data are represented as means (SD). Liquid junction potential: −14 mV.

last interspike interval divided by the second interspike interval (mean: 0.97 (SD: 0.86); Fig. 3*F* and Table 1). A comparison of each of the active and passive electrical properties of the VP interneurons between the small soma-type and large soma-type identified above revealed no significant difference (*P*-values: resting membrane potential, 0.2601; input resistance, 0.0954; tau, 0.7387; membrane capacitance, 0.0694; minimum current for AP, 0.5043; AP threshold, 0.0819; first AP half-width, 0.1581; last AP half-width, 0.1077; ln(last ISI/second ISI), 0.4701; V_{sag}, 0.2857; two-tailed Mann–Whitney test; significance set to $P < 0.05$). However, 42% of the small soma-type interneurons tested with strong hyperpolarizing current injection did display rebound bursts, while none displayed this behaviour in the large soma-type neurons. These findings are similar to those reported for dLGN interneurons (Leist *et al*. 2016) and may support the separation of these interneurons into two morphological types with differences in bursting behaviour.

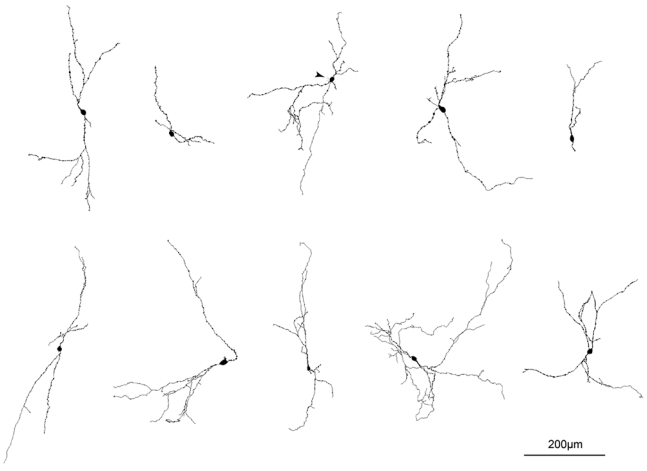

Figure 2. Partial reconstructions of VP interneurons
3D reconstructed partial morphologies. Putative axons are coloured grey and also marked with arrowhead.

Synaptic connections formed by VP interneurons

We obtained recordings of synaptically connected pairs of neurons formed by VP interneurons onto TC neurons ($n = 9$ pairs; five in voltage-clamp, four in current-clamp) and by neighbouring VPi neurons ($n = 9$ pairs) using whole-cell multiple patch-clamp with up to four pipettes simultaneously (Fig. 4). Post-synaptic amplitudes onto both TC and VPi neurons displayed moderate short-term synaptic depression (Fig. 4*A*, *C* and *F*). Connection probabilities under these slice conditions for VPi–TC and VPi–VPi pairs were 3.46% and 7.89%, respectively (VPi–TC: $n = 260$ pairs tested; VPi–VPi: $n = 114$ pairs tested; Fig. 4*B* and *E*). Inhibition from a single VPi was sufficiently effective to alter action potentials in neighbouring VPi neurons ($n = 2$; Fig. 4*D*). Short term plasticity quantifications show similar normalized IPSP changes between VPi–TC and VPi–VPi pairs for each stimulation (Fig. 4*F*). Amplitudes, latencies and 20–80% rise times of inhibitory postsynaptic potentials (IPSPs) were not significantly different for VPi–VPi and VPi–TC neuron pairs (*P*-values: IPSP amplitude, 0.0503; 20–80% rise time, 0.9399; latency, 0.1147; two-tailed Mann–Whitney test; significance set to $P < 0.05$), but IPSPs in VPi–VPi pairs exhibited a significantly longer decay time constant (*P*-value: decay, 0.0112; two-tailed Mann–Whitney test; significance set to $P < 0.05$; Fig. 4*G*).

Save for a significant difference in VPi–VPi IPSP amplitude, the VPM or VPL patched location did not show any significant differences in IPSP features for VPi–VPi pairs (*P*-values: IPSP amplitude, 0.0317; 20–80% rise time, 0.4127; latency, 0.9048; decay, 0.9048) and VPi–TC pairs (*P*-values: IPSP amplitude, 0.3333; 20–80% rise time, 1.000; latency, 0.6667; decay, 0.3333). One paired recording originated from a pre-weaned (<P21) mouse and therefore an analysis of differences based on age was not completed.

A sequence of inhibition involving three VPis was recorded (Fig. 5*A* and *B*) in dorsal VP (Fig. 5*E*). VPi–TC and VPi–VPi neuronal pairs revealed putative dendro-dendritic and dendro-somatic appositions under light microscopy (i.e. physical touch under ×100 magnification) (Fig. 5*C* and *D*). VPi–TC and VPi–VPi soma pairs were localized near the centre of VP (Fig. 5*F* and *G*). The TC neurons in Fig. 5*C* and *D* have their primary dendrites arranged in a semicircle around the soma, analogous to the W-like dendritic arborization of the X-, W-, and Y-like morphological types in the dLGN (McAllister & Wells, 1981; Sherman & Spear, 1982; Krahe

et al. 2011). In dLGN, X cells have been found to be the major postsynaptic target of interneurons (Mastronarde, 1987; Humphrey & Weller, 1988; Saul & Humphrey, 1990). This may allude to a possible deviation from the dLGN microcircuitry.

Inhibition in the VP nucleus

We aimed to elucidate the microcircuitry surrounding VPi feedforward inhibition by analysing medial lemniscus (ML) stimulation amplitudes and the timing of their evoked postsynaptic currents in voltage-clamped TC

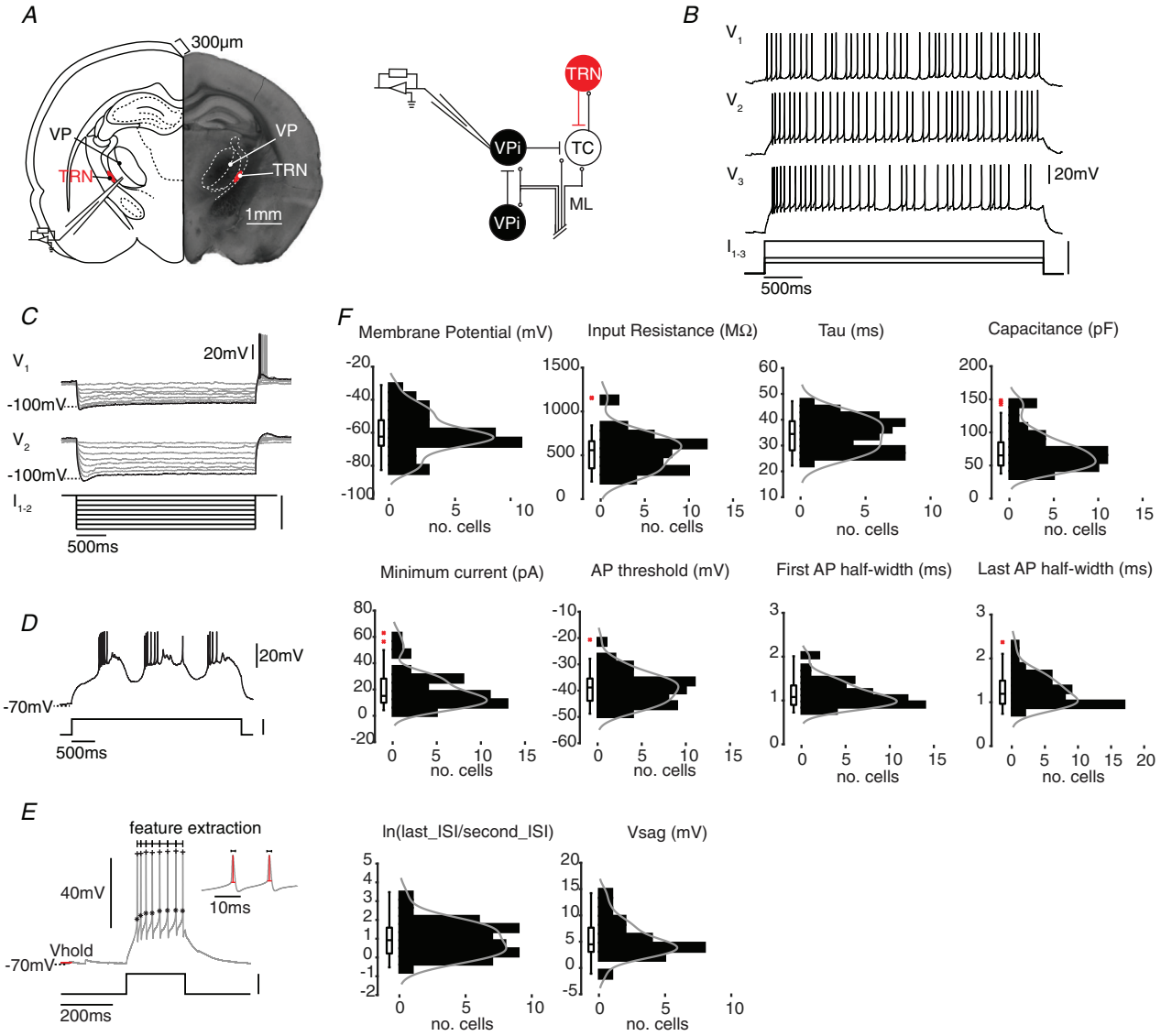

Figure 3. Electrophysiology of VP interneurons
A, left, example 300 μm coronal slice. Right, relevant cell populations and axon tract. *B*, firing pattern at three different holding potentials, V_1: −60 mV, V_2: −70 mV, V_3: −80 mV. $I_{1–3}$: current injected for V_1 (10 pA), V_2 (14.4 pA), V_3 (30 pA). Scale bar: 30 pA. *C*, hyperpolarizing current steps of 10 pA increments for V_1 and 11 pA increments for V_2 ($I_{1–2}$). Scale bar: 70 pA for V_1, 77 pA for V_2. *D*, example trace of a spontaneously oscillating interneuron. Scale bar: 24 pA. *E*, feature extraction analyses of one example trace. Red line represents average voltage value of the initial 200 ms. AP peak shown with '+', AP threshold with '∗'. Interspike intervals at top of trace. AP width shown in zoomed portion of the trace to the right. Scale bar: 31.2 pA. *F*, 10 active and passive electrophysiological features in histograms (bin = 10) and boxplots. Membrane potential (n = 37 cells), input resistance (n = 52 cells), tau (n = 52 cells), capacitance (n = 52 cells), minimum current (n = 47), AP threshold (n = 53 cells), first AP half-width (n = 53 cells), last AP half-width (n = 53 cells), ln(last ISI/first ISI) (n = 50 cells), V_{sag} (n = 25 cells). Non-parametric estimations of distribution shown as a grey line. Outliers in red x are greater than 1.5 quartiles. None of the distributions are gaussian (Kolmogorov–Smirnov test; $P < 0.05$). ML, medial lemniscus; TC, thalamocortical relay; TRN, thalamic reticular nucleus; VPi, VP interneuron.

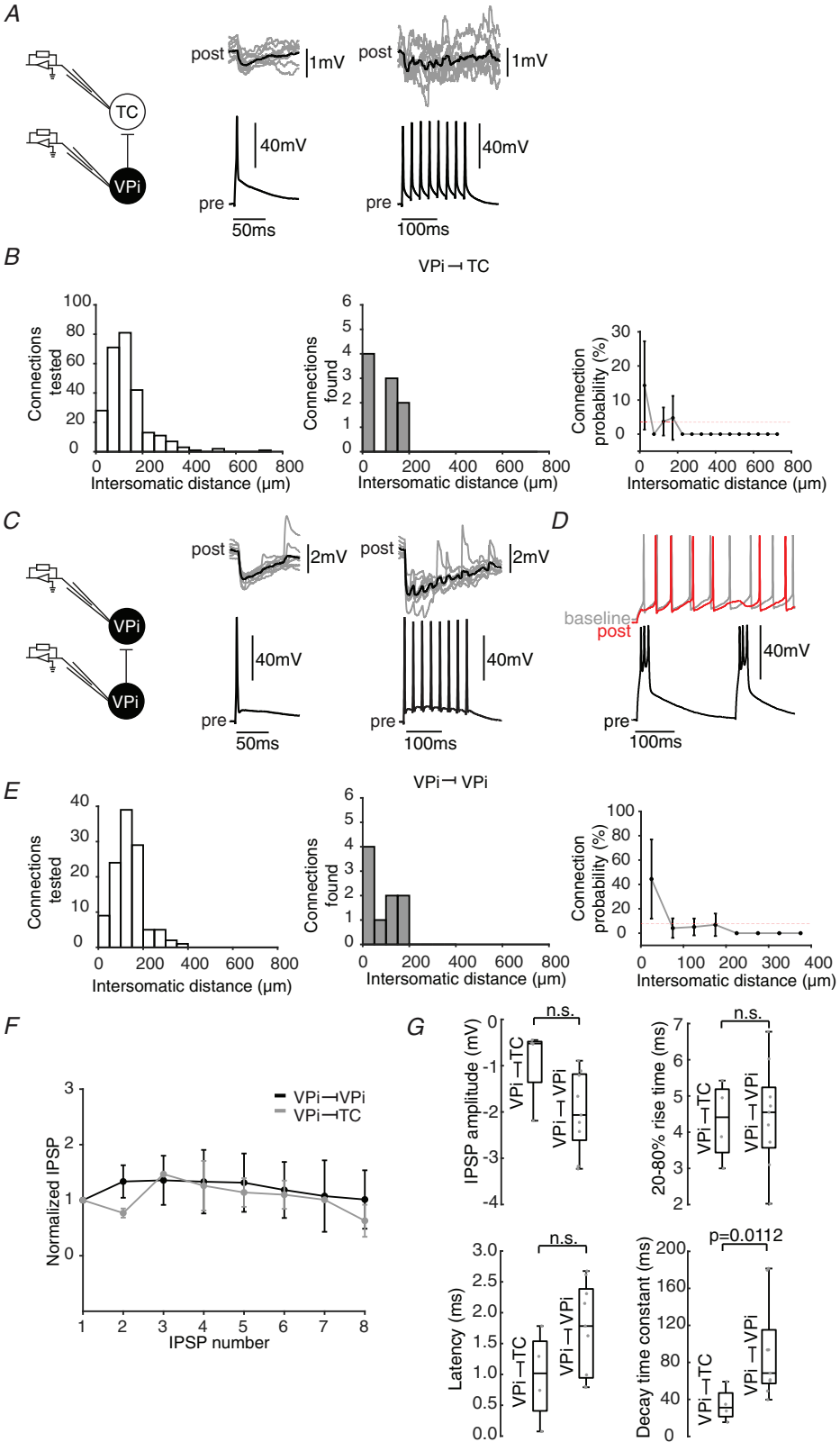

Figure 4. Synaptic connections formed by VP interneurons
A, left, whole-cell paired recordings of presynaptic VPi, postsynaptic TC. Right, single presynaptic VPi actional potential and postsynaptic TC IPSPs (black: average of 10 traces; current clamp V_{hold}: −50 mV). *n* = 4 paired

recordings current clamp, n = 5 paired recordings voltage clamp. Train of action potentials (black: average of 8 traces). *B*, connections tested, connections found, and connection probabilities per intersomatic distances for VPi–TC pairs. Red dashed line represents global probability (3.46%). Error bars represent 95% binomial confidence interval. *C*, left, whole-cell paired recordings of presynaptic VPi, postsynaptic VPi. Right, single presynaptic VPi action potential and postsynaptic VPi IPSPs (black: average of 10 traces; current clamp V_{hold}: −50 mV). n = 9 paired recordings current clamp. Train of action potentials (black: average of 8 traces). *D*, presynaptic VPi delaying and preventing an action potential in postsynaptic VPi (n = 2 pairs). *E*, as in *C* for VPi–VPi pairs. Red dashed line represents global probability (7.89%). *F*, normalized IPSP for each stimulation in a 40 Hz train. Trains recorded with other stimulation frequencies were not included (n = 2 VPi–TC pairs, n = 7 VPi–VPi pairs). *G*, IPSP amplitude: VPi–VPi: −2.00 (0.86) mV, VPi–TC: −0.92 (0.85) mV, 20–80% rise time: VPi–VPi: 4.46 (1.44) ms, VPi–TC: 4.31 (1.09) ms, latency: VPi–VPi: 1.75 (0.75) ms, VPi–TC: 0.97 (0.73) ms, and decay time constants: VPi–VPi: 91.87 (53.39) ms, VPi–TC: 34.20 (18.47) ms. *P*-values: 0.0503, IPSP amplitude; 0.9399, 20–80% rise time; 0.1147, latency; 0.0112, decay. n.s.: not significant, Mann–Whitney U-test, *P*-value < 0.05. Data are presented as means (SD).

neurons. In particular, we addressed whether VPis form triadic and non-triadic structures in the same way as observed in the dLGN (Hamos *et al.* 1985; Morgan & Lichtman, 2020). The ML is an axon tract terminating in the VP which carries sensory information from the face and body (Lund & Webster, 1967; Dörfl, 1985; Cliffera & Giesler, 1989; Pierret *et al.* 2000; Veinante *et al.* 2000). We established a preparation to stimulate the sensory input via the ML using horizontally oriented slices of the VP (Fig. 6*A*). To verify that VPis receive ML input, we recorded EPSPs received by VPis during ML bipolar electrode stimulation (Fig. 6*B*) and confirmed that they were mediated by glutamate receptor activation by bath applying 6-cyano-7-nitro-quinoxaline-2,3-dione (CNQX) and D-(−)-2-amino-5-phosphonopentanoic acid (DAP5) (10 μM GluR block; n = 4 cells block, n = 3 cells block and washout). The EPSPs displayed short-term synaptic depression (Fig. 6*B*). To ensure local feedforward inhibition of TC neurons, we excised the TRN (Fig. 6*C*) to eliminate the possibility of invoking feedback inhibition. By holding TC neurons at +10 mV, we observed ML evoked local inhibitory postsynaptic currents (IPSCs) (Fig. 6*D*). To exclude direct electrical excitation of inhibitory axons or dendrites from further experiments as opposed to glutamatergic activation, we bath-applied CNQX and DAP5 (Fig. 6*D*). The glutamatergic receptor blockers abolished the delayed trains of IPSCs confirming that the IPSCs were generated synaptically via ML stimulation of VP interneurons (Fig. 6*D*; n = 3 cells 10 μM GluR block).

Electrical stimulation of the ML can activate many axons depending on the stimulation current amplitude and threshold of activation for each axon. Monosynaptic EPSCs and disynaptic IPSCs in TC neurons due to ML stimulation will arise from only one of two possible sources: monosynaptic excitation and disynaptic inhibition resulting from the activation of the same ML axon, or the activation of different ML axons. It therefore follows that we can discriminate these two outcomes by monitoring whether the current thresholds for EPSC or IPSC activation are the same or different. Thus, we increased the amplitude of ML stimulation in increments of 1 or 0.5 μA and observed monosynaptic excitatory and disynaptic inhibitory postsynaptic currents in the patched TC neuron held at −70 and +10 mV, respectively (Fig. 6*E* and *F*). Our collected results are typified in cells shown in Fig. 6*E* and *F*. In our first example (Fig. 6*E*), disynaptic IPSCs and monosynaptic EPSCs are induced at the same current threshold. This is observed as a step increase in IPSC and EPSC amplitude as a function of current amplitude (Fig. 6*E*). In a different subset of cells, a different threshold of ML stimulation elicited IPSCs and EPSCs (Fig. 6*F*; same threshold: n = 8 EPSC–IPSC pairs, different threshold: n = 11 EPSC–IPSC pairs, from n = 17 cells). In this cell, IPSC amplitudes continued to increase as a function of current amplitude while the EPSC amplitudes progressed as one distinct step increase (Fig. 6*F*). There is no distinct increase in IPSC amplitude at EPSC activation threshold (Fig. 6*F*). The IPSC onset time subtracted by the EPSC onset time for the same threshold experiments remained reliably around 1 ms (mean: 0.73 (SD: 0.62) ms) whereas the inhibitory delay in different threshold experiments had a much wider range of latencies (mean: 0.54 (SD: 3.54) ms) (Fig. 6*E*–*G*), likely due to conduction velocity differences between ML axons and different latencies of interneuron recruitment.

These experiments indicate that two different circuit arrangements are present in VP. The fast and reliable feedforward inhibition seen in the same threshold experiments indicates a triadic circuit arrangement (Fig. 6*H*), which has been reported in the dLGN (Hamos *et al.* 1985; Morgan & Lichtman, 2020), and the more variable feedforward inhibition, suggested by the different threshold experiments, indicates a classic local lateral inhibition (Fig. 6*I*). The results are similar to those found in dLGN that show 'locked' (same threshold) and 'non-locked' (different threshold) inhibition in response to optic tract stimulation (Blitz & Regehr, 2005). It is therefore possible that processing of these two different sensory modalities, and perhaps others, uses common circuits and stereotypical computations for their subcortical sensory processing.

Disinhibition in the VP nucleus

Given the anatomical evidence for dLGN interneurons forming diverse synaptic circuit motifs with triadic structures (Morgan & Lichtman, 2020) and for VPi–VPi connected pairs as a mechanism of disinhibition (Fig. 4), we aimed to determine whether VPis also formed triadic and non-triadic feedforward disinhibitory circuits. We first tested whether TRN excision from the experimental preparation is necessary by stimulating the TRN while simultaneously recording the VPi response in whole-cell mode ($n = 2$ cells 10 μM gabazine block and washout; Fig. 7*A*–*C*). The synaptic delay from stimulation to onset of the first IPSC was mean 3.65 (SD: 1.07) ms and mean 3.32 (SD: 2.66) ms ($n = 5$ traces; Fig. 7*C*), indicative of a monosynaptic inhibitory connection onto the VP interneurons from the TRN. Therefore, we removed the TRN from the slice preparations to allow further investigation of feedforward disinhibition from local interneurons exclusively. Short term plasticity quantification shows a clear depressing change in normalized IPSC values (Fig. 7*D*). We used a similar approach to find excitatory cortical input onto VP interneurons ($n = 4$ cells 10 μM GluR block and washout, $n = 4$ cells 10 μM GluR block; Fig. 7*E*–*H*). Cortical inputs displayed short term synaptic facilitation which enabled their distinction from depressing ML inputs (Figs 7*G* and *H*, and 6*B*).

In a similar set of experiments to the ones previously described, we patched each VPi in voltage-clamp and

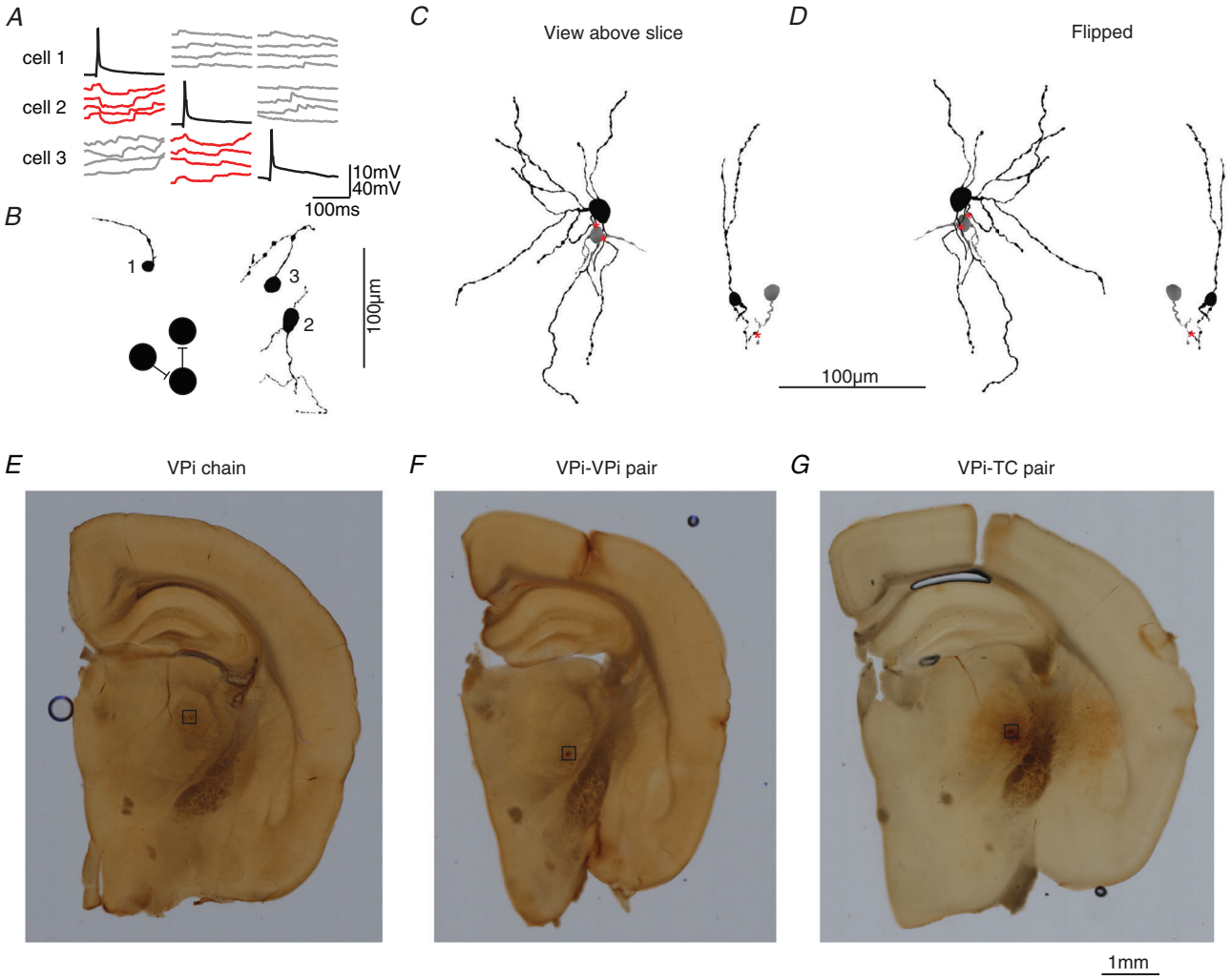

Figure 5. Locations of paired recordings
A, pre- and postsynaptic responses from three simultaneously patched neurons. Presynaptic spikes in black, postsynaptic connections in red. Non-connected responses in grey. *B*, partial reconstructions of experiment shown in *A*. *C*, partial reconstructions of a VPi to TC pair (left) and VPi to VPi pair (right). Presynaptic neuron in grey, postsynaptic neuron in black. Putative touch locations marked with a red asterisk. *D*, same as in *C*, flipped. *E*, slice of partial reconstructions shown in *A* and *B*. *F*, slice of paired reconstruction shown in *C* and *D* left. *G*, slice of paired reconstruction shown in *C* and *D* right.

observed monosynaptic EPSCs and disynaptic IPSCs upon increasing ML stimulation in increments of 1 or 0.5 μA (Fig. 8*A*). Analogous to the feedforward inhibition experiments, a same and different threshold dichotomy was observed (Fig. 8*B* and *C*). In a subset of experiments, an IPSC and EPSC were obtained with the same current threshold. In all other experiments, different thresholds were required for observing an IPSC and an EPSC (same threshold: n = 5 EPSC–IPSC pairs, different threshold: n = 14 EPSC–IPSC pairs, from n = 17 cells; Fig. 8*B* and *C*). The IPSC onset time subtracted by the EPSC onset time in the same threshold experiments remained reliably around 1 ms (mean: 1.24 (SD: 0.67) ms), whereas the different threshold experiments displayed much more varied delays in inhibition (mean: 2.59 (SD: 2.05) ms; Fig. 8*B*–*D*). This is indicative of triadic (Fig. 8*E*) and non-triadic (Fig. 8*F*) disinhibitory circuit arrangements, as observed anatomically in the dLGN (Morgan & Lichtman, 2020),

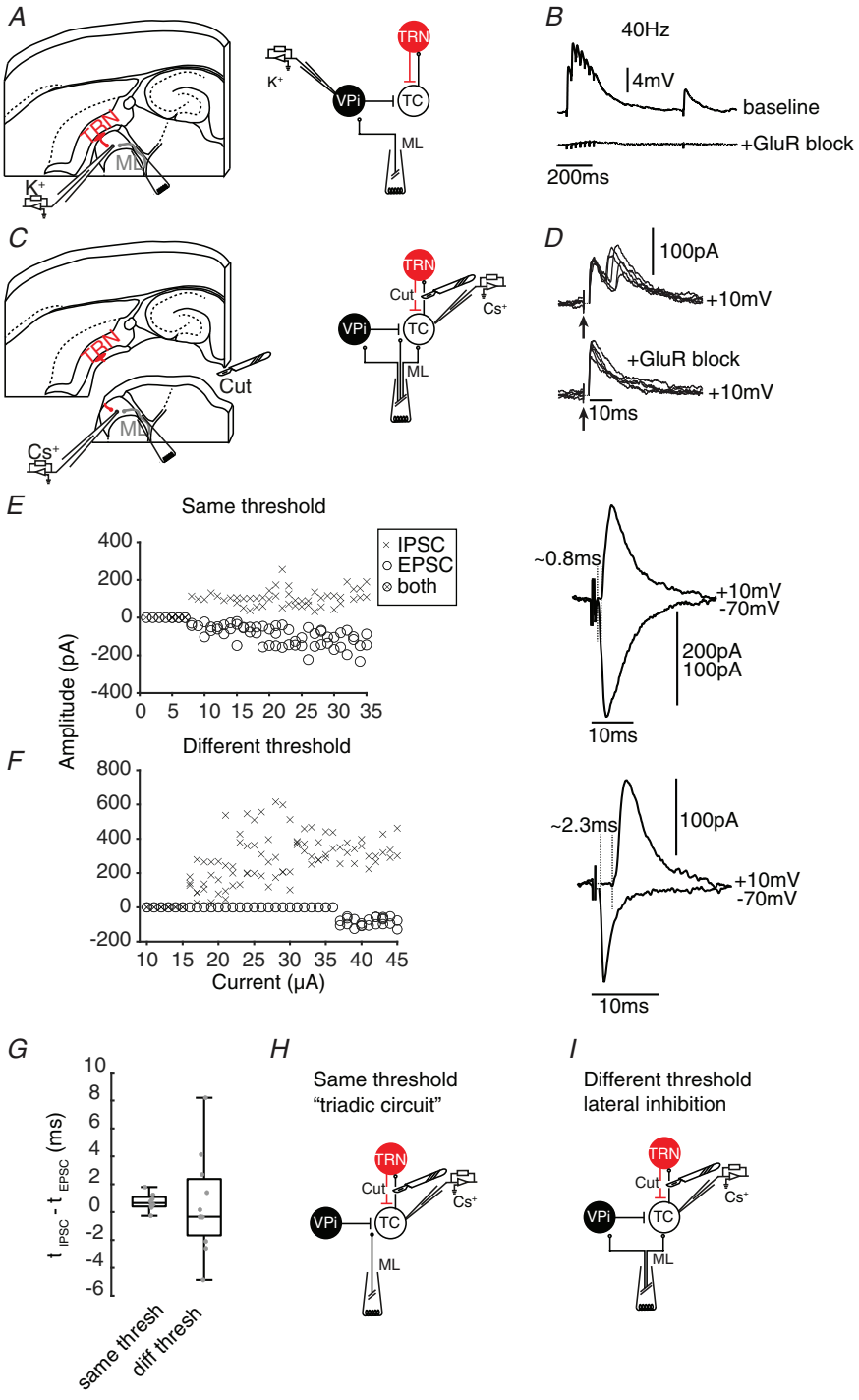

Figure 6. VP interneurons receive sensory input and provide two forms of feedforward inhibition
A, a bipolar electrode is placed on the medial lemniscus (ML) and a VPi is patched with regular ICS in current clamp. *B*, EPSPs seen in VPi following ML stimulation. EPSPs are blocked by the application of glutamatergic receptor blockers (GluR block: CNQX, DAP5 10 μM; n = 4 cells). *C*, same set-up as in *A*, with a relay patched in voltage clamp with caesium ICS and TRN separated from VP. *D*, multiple IPSCs seen with ML pulse stimulation. Delayed IPSCs abolished with GluR block, but first IPSC resulting from direct electrode stimulation remains. *E*, left, amplitude of EPSC or IPSC against current threshold. Right, example IPSC and EPSC from ML stimulation (overlay). *F*, left, amplitude of EPSC or IPSC against current threshold. Right, another example as in *E*. *G*, time delay difference of IPSCs and EPSCs for same threshold experiments (n = 8 EPSC–IPSC pairs, 0.73 (0.62) ms) and different (diff) threshold experiments (n = 11 EPSC–IPSC pairs, 0.54 (3.54) ms). *H*, putative circuit arrangement for same threshold experiments. *I*, putative circuit arrangement for different threshold experiments. Data are expressed as means (SD).

and resembling our finding of a feedforward inhibition circuit motif.

Due to our ability to physiologically differentiate triadic and non-triadic synapses in our previously described feedforward inhibition and feedforward disinhibition studies, responses from trains of ML stimulation can be analysed for each synapse type (Fig. 8*G* and *H*). With 40 Hz ML stimulation trains, TC triadic and non-triadic synapses both exhibit mildly depressing short-term plasticity (Fig. 8*G*). Similarly, VPi triadic and non-triadic normalized EPSC responses show comparable depressing quantifications (Fig. 8*H*). Triadic and non-triadic synapses may have both evolved to permit adaptive mechanisms for repeated stimuli.

Discussion

In this study, we have demonstrated for the first time that VPis play an active role within VP microcircuitry. VPis exhibit a low threshold burst firing pattern and have expansive morphologies, traversing several hundred micrometres. Furthermore, we have identified connected pairs of VPis and TCs and between VPis, the latter providing a source of disinhibition of TC activation. Finally, we have shown that VPis receive direct ML input and we have elucidated two modes of TRN-independent feedforward inhibition and disinhibition delineating VPi's role in shaping incoming signals.

We find striking parallels between the single cell properties and microcircuitry of dLGN and VP interneurons. The initial burst seen in the firing pattern of VP interneurons at low holding potentials is indicative of T-type calcium channels that have a low activating threshold also seen in dLGN interneurons (Hernández-Cruz & Pape, 1989; Pape *et al.* 1994; Williams *et al.* 1996; Zhu *et al.* 1999*b*). Moreover, VPis display a morphology indistinguishable from the bipolar and tripolar morphologies of dLGN interneurons (Zhu & Lo, 1999; Leist *et al.* 2016). Our paired recordings and bipolar stimulation experiments elucidate the same

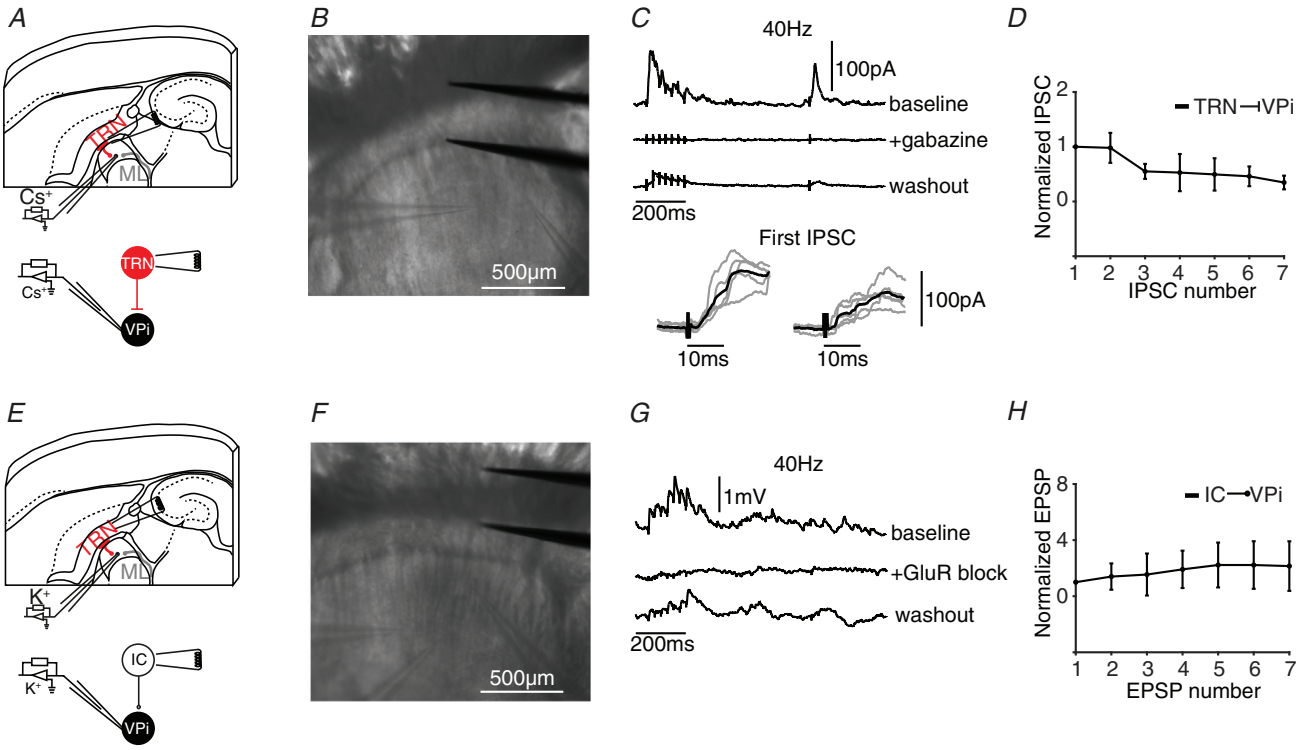

Figure 7. VP interneurons receive input from the reticular nucleus and the cortex
A, schematic representation of experiment with relevant cell populations shown on right. *B*, slice image of experiment. *C*, top, IPSCs displayed in patched VPi upon TRN stimulation at 40 Hz with a recovery pulse (average of 4 traces). IPSCs are abolished with gabazine (10 μM; average of 4 traces) and partially recovered during washout (average of 4 traces) (n = 2 cells, block and partial washout). Bottom, first IPSC of both experiments. Five traces in grey, average trace in black. *D*, normalized IPSC for each stimulation in a 40 Hz train. *E*, schematic representation of experiment with relevant cell populations and axon tract shown on right. *F*, slice image of experiment. *G*, EPSPs displayed in patched VPi upon IC (internal capsule) stimulation at 40 Hz with a recovery pulse (average of 9 traces). EPSPs are abolished with GluR block (CNQX and DAP5; average of 5 traces) and partially recovered during washout (average of 5 traces) (n = 4 cells, block; n = 4 cells, block and partial washout). *H*, normalized EPSP for each stimulation in a 40 Hz train.

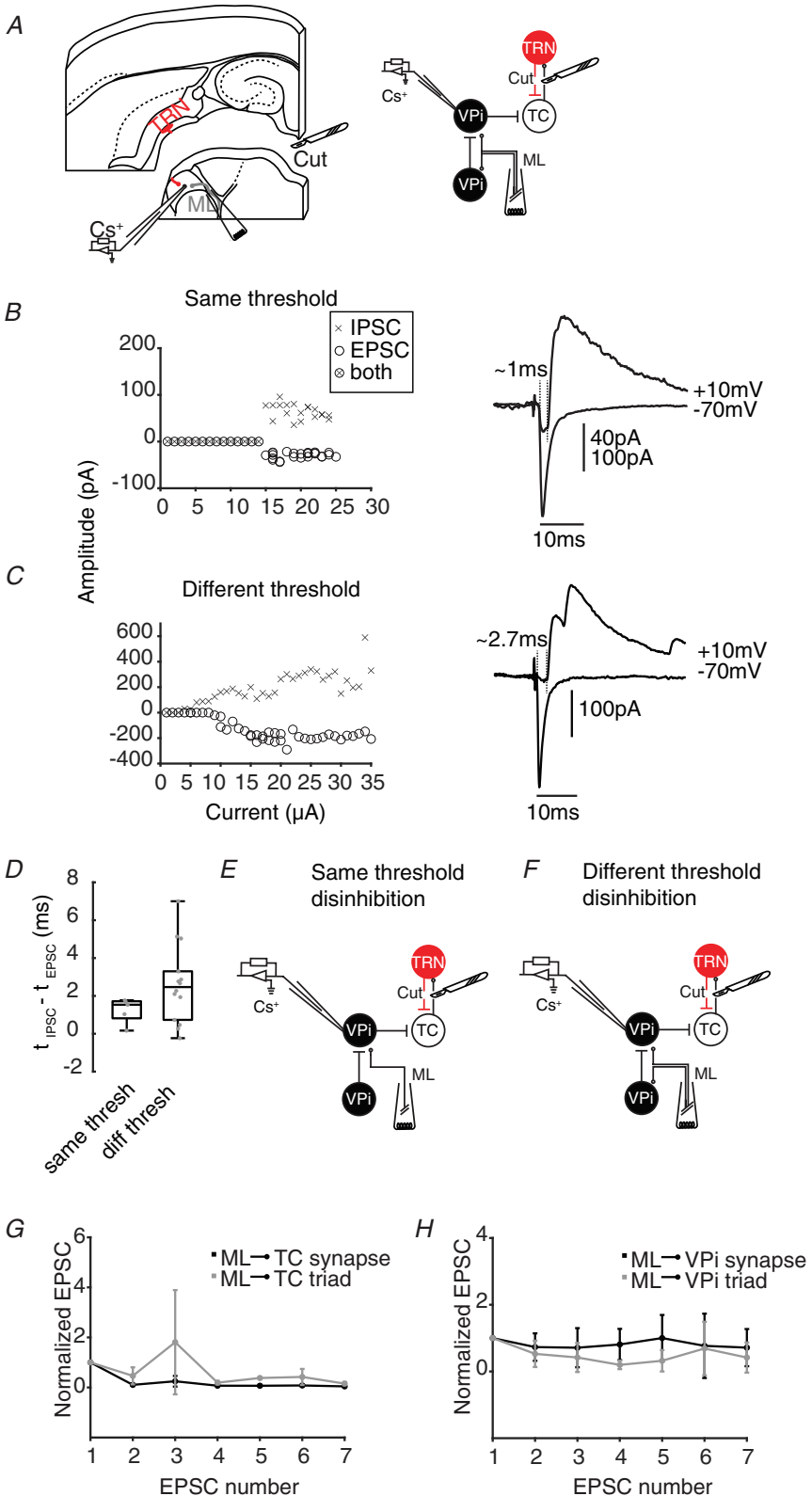

Figure 8. VP interneurons provide two forms of feedforward disinhibition
A, a bipolar electrode is placed on the medial lemniscus (ML) and a VPi is patched with caesium ICS in voltage clamp. *B*, left, amplitude of EPSC or IPSC against current threshold. Right, example IPSC and EPSC from ML stimulation (overlay). *C*, left, amplitude of EPSC or IPSC against current threshold. Right, another example as in *B*. *D*, time delay difference of IPSCs and EPSCs for same threshold experiments (n = 5 EPSC–IPSC pairs, 1.24 (0.67) ms) *vs*. different (diff) threshold experiments (n = 14 EPSC–IPSC pairs, 2.59 (2.05) ms). *E*, putative circuit arrangement for same threshold experiments. *F*, putative circuit arrangement for different threshold experiments. *G* and *H*, normalized EPSC for each stimulation in a 40 Hz train for triadic and non-triadic synapses in feedforward inhibition (*G*) and feedforward disinhibition (*H*) recordings. Trains or paired pulses recorded with other stimulation frequencies were not included (n = 2 ML–TC triad, n = 2 ML–TC synapse, n = 2 ML–VPi triad, n = 4 ML–VPi synapse). Data are expressed as means (SD).

microcircuitry present in the dLGN (Pasik *et al.* 1976; Weber *et al.* 1989; Blitz & Regehr, 2005; Acuno-Goycolea *et al.* 2008; Cox & Beatty, 2017; Yang *et al.* 2017). These similarities could be explained by common embryonic origins in mouse. Unlike cortical interneurons in the telencephalon, dLGN interneurons originate from the tectum (Jager *et al.* 2016) and migrate post-natally in the dorso-caudal to ventro-rostral direction to the dLGN (Golding *et al.* 2014; Jager *et al.* 2016). VP interneurons have been found to share the same developmental markers (Jager *et al.* 2016) indicating a parallel migration of VPis from a common source (Jager *et al.* 2021).

The percentage of local interneurons in the total neuronal population remains the greatest distinction between the dLGN and other first order thalamic nuclei like VP (Arcelli *et al.* 1997; Cavdar *et al.* 2014; Evangelio *et al.* 2018). dLGN interneurons shorten the temporal window of opportunity for integrating sensory information and sharpen receptive fields (Sherman, 2004; Bruno, 2011; Hirsch *et al.* 2015; Heiberg *et al.* 2016); however, perhaps this level of processing is not required in all somatotopic regions of the VP or tonotopic regions of the medial geniculate nucleus, the auditory thalamus, where spatial and temporal refinement of sensory input is not crucial. Interneurons may be concentrated in somatotopic or tonotopic regions where differential processing may be needed, such as for the digits or whisker barreloids, or in evolutionarily relevant auditory cues. TRN feedback inhibition occurs with a longer delay (Pinault, 2004) compared to that of VPi feedforward inhibition, and thus the TRN could be providing a coarser form of inhibitory processing. Thus, sensory information processing in the VP may differ in its relative influence on reticular cells *vs.* interneurons (Arcelli *et al.* 1997).

Further questions remain regarding VPi neuron participation in fundamental thalamic processes such as sleep or pathological oscillatory states. We have shown that, like the TRN, the rhythmic pacemaker of the thalamus (Huguenard & Prince, 1994; McCormick & Bal, 1997; Fogerson & Huguenard, 2016), VPis participate in spontaneous oscillatory activity and rebound bursts. *In vivo* and *in vitro* studies have also shown thalamic interneurons participating in rhythmic behaviour (Deschênes *et al.* 1984; Zhu *et al.* 1999*a*); however, there are conflicting reports for the existence of TRN–VPi synapses (Zhu & Lo, 1999; Campbell *et al.* 2020). The role and origin of these oscillations are enigmatic and call for further investigation. Similarly, the involvement of thalamic local interneurons in pathological oscillatory states, for example in epilepsy, is currently unknown. Investigation of the role of thalamic local interneurons in oscillatory behaviour may provide more insight for a canonical model of thalamic rhythm generation and pathological states.

References

Acuno-Goycolea C, Brenowitz S & Regehr W (2008). Active dendritic conductances dynamically regulate GABA release from thalamic interneurons. *Neuron* **57**, 420–431.

Allen Institute for Brain Science (2004). Allen Mouse Brain Atlas. http://atlas.brain-map.org/

Arcelli P, Frassoni C, Regondi MC, Biasi SD & Spreafico R (1997). GABAergic neurons in mammalian thalamus: a marker of thalamic complexity? *Brain Res Bull* **42**, 27–37.

Babadi B, Casti A, Xiao Y, Kaplan E & Paninski L (2010). A generalized linear model of the impact of direct and indirect inputs to the lateral geniculate nucleus. *J Vis* **10**, 22.

Blitz D & Regehr W (2005). Timing and specificity of feed-forward inhibition within the LGN. *Neuron* **45**, 917–928.

Bruno RM (2011). Synchrony in sensation. *Curr Opin Neurobiol* **21**, 701–708.

Butts D, Weng C, Jin J, Alonso J & Paninski L (2011). Temporal precision in the visual pathway through the interplay of excitation and stimulus-driven suppression. *J Neurosci* **31**, 11313–11327.

Campbell PW, Govindaiah G, Masterson SP, Bickford ME & Guido W (2020). Synaptic properties of the feedback connections from the thalamic reticular nucleus to the dorsal lateral geniculate nucleus. *J Neurophysiol* **124**, 404–417.

Casti A, Hayot F, Xiao Y & Kaplan E (2008). A simple model of retina-LGN transmission. *J Comput Neurosci* **24**, 235–252.

Cavdar S, Bay H, Yildiz S, Akakin D, Sirvanci S & Onat F (2014). Comparison of numbers of interneurons in three thalamic nuclei of normal and epileptic rats. *Neuroscience Bulletin* **30**, 451–460.

Cliffera KD & Giesler GJ (1989). Postsynaptic dorsal column pathway of the rat. III. Distribution of ascending afferent fibers. *J Neurosci* **9**, 3146–3168.

Cox C & Beatty JA (2017). The multifaceted role of inhibitory interneurons in the dorsal lateral geniculate nucleus. *Vis Neurosci* **34**, E017.

Deschênes M, Paradis M, Roy JP & Steriade M (1984). Electrophysiology of neurons of lateral thalamic nuclei in cat: resting properties and burst discharges. *J Neurophysiol* **51**, 1196–1219.

Dörfl J (1985). The innervation of the mystacial region of the white mouse: a topographical study. *J Anat* **142**, 173–84.

Evangelio M, García-Amado M & Clascá F (2018). Thalamocortical projection neuron and interneuron numbers in the visual thalamic nuclei of the adult C57BL/6 mouse. *Front Neuroanat* **12**, 27.

Fogerson M & Huguenard JR (2016). Tapping the brakes: cellular and synaptic mechanisms that regulate thalamic oscillations. *Neuron* **92**, 87–704.

Golding B, Pouchelon G, Bellone C, Murthy S, Nardo AA, Govindan S, Ogawa M, Shimogori T, Lüscher C, Dayer A & Jabaudon D (2014). Retinal input directs the recruitment of inhibitory interneurons into thalamic visual circuits. *Neuron* **81**, 1057–1069.

Hamos JE, Horn SC, Raczkowski D & Sherman DJ (1985). Synaptic connectivity of a local circuit neurone in lateral geniculate nucleus of the cat. *Nature* **317**, 618–621.

Heiberg T, Hagen E, Halnes G & Einevoll GT (2016). Biophysical network modelling of the dLGN circuit: Different effects of triadic and axonal inhibition on visual responses of relay cells. *PLoS Comp Bio* **12**, e1004929.

Hernández-Cruz A & Pape HC (1989). Identification of two calcium currents in acutely dissociated neurons from the rat lateral geniculate nucleus. *J Neurophysiol* **61**, 1270–1283.

Hirsch J, Wang X, Sommer F & Martinez L (2015). How inhibitory circuits in the thalamus serve vision. *Annu Rev Neurosci* **38**, 309–329.

Huguenard JR & Prince DA (1994). Intrathalamic rhythmicity studied in vitro: nominal T-current modulation causes robust antioscillatory effects. *J Neurosci* **14**, 5485–5502.

Humphrey A & Weller R (1988). Structural correlates of functionally distinct X-cells in the lateral geniculate nucleus of the cat. *J Comp Neurol* **268**, 448–468.

Jager P, Moore G, Calpin P, Durmishi X, Salgarella I, Menage L, Kita Y, Wang Y, Kim DW, Blackshaw S, Schultz SR, Brickley S, Shimogori T & Delogu A (2021). Dual midbrain and forebrain origins of thalamic inhibitory interneurons. *Elife* **10**, e59272.

Jager P, Zhiwen Ye XY, Zagoraiou L, Prekop H-T, Partanen J, Jessell TM, Wisden W, Brickley SG & Delogu SG (2016). Tectal-derived interneurons contribute to phasic and tonic inhibition in the visual thalamus. *Nat Commun* **7**, 13579.

Krahe T, El-Danaf R, Dilger E, Henderson S & Guido W (2011). Morphologically distinct classes of relay cells exhibit regional preferences in the dorsal lateral geniculate nucleus of the mouse. *J Neurosci* **31**, 17437–17448.

Lee S-C, Cruikshank SJ & Connors BW (2010). Electrical and chemical synapses between relay neurons in developing thalamus. *J Physiol* **588**, 2403–2415.

Leist M, Datunashvilli M, Kanyshkova T, Zobeiri M, Aissaoui A, Cerina M, Romanelli MN, Pape H-C, Budde T (2016). Two types of interneurons in the mouse lateral geniculate nucleus are characterized by different h-current density. *Sci Rep* **6**, 24904.

Lund RD & Webster KE (1967). Thalamic afferents from the dorsal column nuclei: an experimental anatomical study in the rat. *J Comp Neurol* **130**, 301–311.

Martinez L, Molano-Mazón M, Wang X, Sommer F & Hirsch J (2014). Statistical wiring of thalamic receptive fields optimizes spatial sampling of the retinal image. *Neuron* **81**, 943–956.

Mastronarde D (1987). Two classes of single-input X-cells in cat lateral geniculate nucleus. II. Retinal inputs and the generation of receptive-field properties. *J Neurophysiol* **57**, 381–413.

McAllister J & Wells J (1981). The structural organization of the ventral posterolateral nucleus in the rat. *J Comp Neurol* **197**, 271–301.

McCormick DA & Bal T (1997). Sleep and arousal: thalamocortical mechanisms. *Annu Rev Neurosci* **20**, 185–215.

Morgan JL & Lichtman JW (2020). An individual interneuron participates in many kinds of inhibition and innervates much of the mouse visual thalamus. *Neuron* **106**, 468–481.e2.

Pape HC, Budde T, Mager R & Kisvárday ZF (1994). Prevention of Ca^{2+}-mediated action potentials in GABAergic local circuit neurones of rat thalamus by a transient K^{+} current. *J Physiol* **478**, 403–422.

Pasik P, Pasik T & Hámori J (1976). Synapses between interneurons in the lateral geniculate nucleus of monkeys. *Exp Brain Res* **25**, 1–13.

Perin R & Markram H (2013). A computer-assisted multi-electrode patch-clamp system. *J Vis Exp* **80**, e50630.

Pierret T, Lavallée P & Deschênes M (2000). Parallel streams for the relay of vibrissal information through thalamic barreloids. *J Neurosci* **20**, 7455–7462.

Pinault D (2004). The thalamic reticular nucleus: structure, function and concept. *Brain Res Rev* **46**, 1–31.

Saul AB & Humphrey AL (1990). Spatial and temporal response properties of lagged and nonlagged cells in cat lateral geniculate nucleus. *J Neurophysiol* **64**, 206–224.

Sherman S (2004). Interneurons and triadic circuitry of the thalamus. *Trends Neurosci* **27**, 670–675.

Sherman S & Spear P (1982). Organization of visual pathways in normal and visually deprived cats. *Physiol Rev* **62**, 738–855.

Simko J (2021). single_cell_dataset.zip. Figshare dataset: https://doi.org/10.6084/m9.figshare.15046914.v1

Tamamaki N, Yanagawa Y, Tomioka R, Miyazaki J, Obata K & Kaneko T (2003). Green fluorescent protein expression and colocalization with calretinin, parvalbumin, and somatostatin in the GAD67-GFP knock-in mouse. *J Comp Neurol* **467**, 60–79.

Trang N, Choisy M, Nakagomi T, Chinh N, Doan Y, Yamashiro T, Bryant JE, Nakagomi O, Anh D (2015). Determination of cut-off cycle threshold values in routine RT-PCR assays to assist differential diagnosis of norovirus in children hospitalized for acute gastroenteritis. *Epidemiol Infect* **143**, 3292–3299.

Veinante P, Jacquin MF & Deschênes M (2000). Thalamic projections from the whisker-sensitive regions of the spinal trigeminal complex in the rat. *J Comp Neurol* **420**, 233–243.

Wang X, Sommer F & Hirsch J (2011). Inhibitory circuits for visual processing in thalamus. *Curr Opin Neurobiol* **21**, 726–733.

Weber AJ, Kalil RE & Behan M (1989). Synaptic connections between corticogeniculate axons and interneurons in the dorsal lateral geniculate nucleus of the cat. *J Comp Neurol* **289**, 156–164.

Williams S, Turner J, Anderson C & Crunelli V (1996). Electrophysiological and morphological properties of interneurones in the rat dorsal lateral geniculate nucleus *in vitro*. *J Physiol* **490**, 129–147.

Yang S, Govindaiah G, Lee S-H, Yang S & Cox CL (2017). Distinct kinetics of inhibitory currents in thalamocortical neurons that arise from dendritic or axonal origin. *PLoS One* **12**, e0189690.

Zhu JJ & Lo F-S (1999). Three GABA receptor-mediated postsynaptic potentials in interneurons in the rat lateral geniculate nucleus. *J Neurosci* **19**, 5721–5730.

Zhu JJ, Lytton WW, Xue JT & Uhlrich DJ (1999*a*). An intrinsic oscillation in interneurons of the rat lateral geniculate nucleus. *J Neurophysiol* **81**, 702–711.

Zhu J, Uhlrich D & Lytton W (1999*b*). Burst firing in identified rat geniculate interneurons. *Neuroscience* **91**, 1445–1460.

Additional information

Data availability statement

The data that support the findings of this study are available from the corresponding author upon reasonable request. Single cell electrophysiology data is openly available at: https://doi.org/10.6084/m9.figshare.15046914.v1 (Simko, 2021).

Competing interests

The authors declare no competing interests.

Author contributions

J.S. and H.M. conceived the project and designed all experiments. J.S. conducted and analysed all electrophysiological data. J.S. performed all paired reconstructions. H.M. supervised all aspects of the work. J.S. created all figures. Both authors edited and revised the manuscript. Both authors have read and approved the final version of this manuscript and agree to be accountable for all aspects of the work in ensuring that questions related to the accuracy or integrity of any part of the work are appropriately investigated and resolved. All persons designated as authors qualify for authorship, and all those who qualify for authorship are listed.

Funding

This study was supported by funding to the Blue Brain Project, a research center of the École polytechnique fédérale de Lausanne (EPFL), from the Swiss government's ETH Board of the Swiss Federal Institutes of Technology.

Acknowledgements

The authors thank our colleague Rajnish Ranjan for the use of his code for electrophysiological feature extraction. The authors also thank our colleagues Deborah La Mendola for her histological expertise and Ying Shi for her efforts in overseeing morphological reconstructions for this project.

Open access funding provided by Ecole Polytechnique Federale de Lausanne.

Keywords

inhibition, interneurons, microcircuitry, mouse, somatosensory thalamus, triadic

Supporting information

Additional supporting information can be found online in the Supporting Information section at the end of the HTML view of the article. Supporting information files available:

Peer review history
Statistical summary document